PHYSICAL REVIEW B **78**, 174421 (2008)

Rationale for femtosecond magnetism explored with x-ray core-hole excitation

L. Braicovich[1] and G. van der Laan[2]
[1]*Dipartimento di Fisica, INFM-CNR-SOFT, Politecnico di Milano, p. Leonardo da Vinci 32, I-20133 Milano, Italy*
[2]*Diamond Light Source, Chilton, Didcot OX11 0DE, United Kingdom*

(Received 5 July 2008; revised manuscript received 5 October 2008; published 20 November 2008)

In magnetic metals the core-hole excitation by x rays leads to a sudden creation of an impurity that is screened in a spin-dependent way. A scattering experiment in the L_3 region terminating with a 3s hole has already been shown to give information on the time scale of this screening process. Here we present a linear-rate model for the analysis of such experiments and apply this to Ni, Co, and Fe metals. This model yields quantitative results that could not be obtained before using an empirical model. The screening time constant in Ni (most likely ~1.5 fs) is definitely longer than in Fe, which presumably is caused by narrow-band effects. The screening time is 0.43 fs in Co, while 0.18 fs is an upper limit in Fe metal. In agreement with the experiment, the model clarifies the variation in the dichroism due to the competition between the core-hole decay and the time it takes to accumulate the screening charge. Finally, the perspectives of this approach are briefly discussed including the importance of future experiments on diluted magnetic impurities.

DOI: 10.1103/PhysRevB.78.174421 PACS number(s): 75.50.−y, 78.70.En, 78.70.Ck, 78.70.Dm

I. INTRODUCTION

The interest in fast dynamics of magnetic systems is rapidly growing. The basic scientific interest is largely due to the possibility of studying the dynamic coupling between different degrees of freedom, such as spin and orbital moments and lattice vibrations.[1–8] Moreover magnetic switching at 40 fs by optical excitation has recently been demonstrated.[9] On the other hand these studies, although not immediately related to applications, belong to a field where spintronics has an increasing technological impact.[10] Besides Ref. 9 the experiments quoted above (and those cited therein) are carried out in "pump-probe" mode taking advantage of short-pulsed laser sources used to excite the specimen. These studies will greatly benefit from new sources offering a short pulse time structure, namely, tabletop attosecond lasers[11–13] and free-electron lasers. The attosecond lasers have already been applied to solid-state spectroscopy[14] but to the authors' knowledge not yet to magnetic solids. The free-electron lasers under implementation will give routine access in the x-ray range to inner-shell spectroscopies in the femtosecond range.[15] At present in core-electron excitation of magnetic systems a pioneering step forward[7] is the use of 100 fs x-ray pulses obtained by slicing of synchrotron radiation pulses. In core spectroscopy an innovative complementary approach, useful around a few femtoseconds down to typically 100 as, was introduced by us and our co-workers in Ref. 16 (hereafter referred to as paper I), where we applied the method of the so-called core-hole clock[17] to femtosecond magnetism in metallic Fe, Co, and Ni. In essence, the system is excited with x rays by creating a core hole, i.e., by initiating suddenly a kind of impurity which decays with the core-hole lifetime τ_c. On this time scale a spin-dependent screening of the impurity occurs with a characteristic time constant τ_s. Whether the screening is complete or incomplete depends on the competition between the two time scales, generating in favorable conditions a situation intermediate between the two limiting cases of no screening ($\tau_c \ll \tau_s$) and full screening ($\tau_c \gg \tau_s$). As explained in paper I and summarized here in Sec. II, it is possible, in a suitable type of scattering experiment, to observe this situation so that *one can obtain unique information on the dynamics of screening of impurities in magnetic systems*. This is probably the fastest process involved in the dynamics of magnetic systems. In particular, we showed in paper I that this screening is incomplete in Ni metal and we related the slower screening compared to Fe to the narrow-band effect of the 3d hole in Ni metal.

In paper I we also introduced an empirical model for the interpretation of the data. This model was merely based on a conjecture, so that its validity is limited and its internal consistency remained an open question. The aim of the present paper is to introduce an improved model on a firmer conceptual basis that is derived from a linear-rate equation. This improved model allows a more realistic discussion of the experimental results of paper I, obtaining different results on the screening time in the range down to a fraction of a femtosecond. Moreover, the improved model gives a solid foundation to the entire topic and implies future research lines that are briefly discussed.

Since the application of the core-hole clock to femtosecond magnetism is still in its infancy, we summarize for clarity the basic concepts and the experimental background in Sec. II. This section is divided into different subsections to enable the reader to navigate through the specifics of the underlying principles. The linear-rate model is presented in Sec. III, also organized in subsections, and includes a comparison with the old empirical model. In the discussion (Sec. IV) we analyze the experimental results of paper I and present briefly some perspectives. The conclusions are summarized in Sec. V.

II. BACKGROUND INFORMATION

The model presented here should be placed in the framework of previous results. This is done in the present section, which is organized into subsections that summarize the dif-

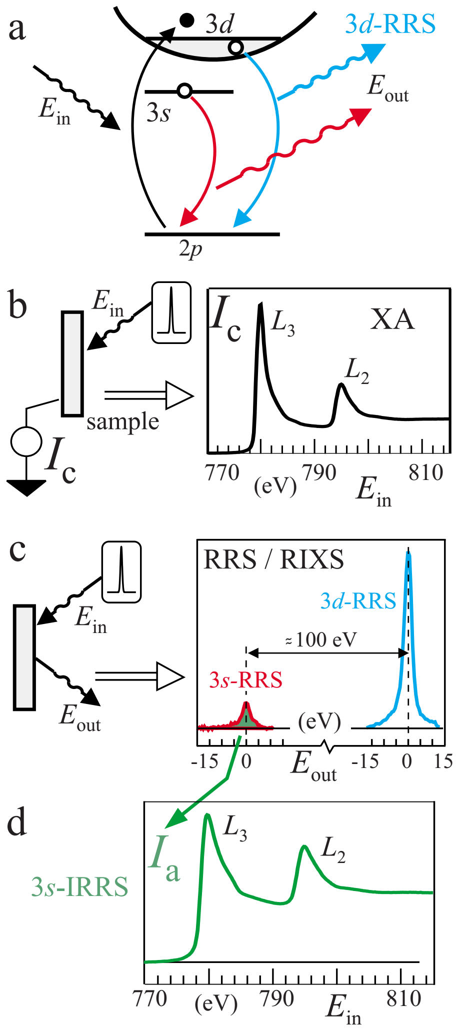

FIG. 1. (Color online) (a) Schematics of resonant x-ray scattering in a transition-metal system showing the decay via the $3d$ valence channel (in blue) and $3s$ inner-shell channel (in red). (b) X-ray-absorption (XA) setup and Co $L_{2,3}$ spectrum of Co metal. (c) Resonant Raman-scattering (RRS) setup and spectrum from Co metal excited at the L_3 peak comprising the $3d$-RRS (blue) and the $3s$-RRS (red). (d) Integrated intensity of the $3s$-RRS as a function of incident-photon energy, which we call the $3s$-integrated resonant Raman scattering (IRRS) of Co metal.

ferent principles behind the technique in order of increasing specialization.

A. Integrated resonant Raman-scattering method

We first discuss the nature of the spectroscopy used in our work. As an example and reference case, we use Co metal (from paper I) but the presentation deals with the general aspects of the experimental method common to all transition-metal systems. The generalization to other systems such as rare earths is easy and not discussed here.

Let us consider first the relevant electronic levels shown schematically in Fig. 1(a), where spin-orbit splitting has been neglected for simplicity. The inelastic-scattering event is initiated by the resonant excitation of the $2p \to 3d$ transition creating a core $2p$ hole and an extra electron in the $3d$ manifold. This excited state has two radiative ways to decay so that there are two x-ray-scattering channels. One is by filling the core hole with a $3d$ electron so that in the final state a valence electron-hole pair is created [decay in blue in Fig. 1(a)]. The other is an inner-shell process in which a $3s$ electron decays to the $2p$ state so that the final state contains an extra $3d$ electron and a $3s$ shallow core hole [decay in red in Fig. 1(a)].

If no selection of the decay products of the core hole is made and all decay products (photons and electrons) are observed, one obtains a measurement for the number of core holes. It is well established that to good approximation the total drain current I_c from the sample is proportional to the total number of core holes. If monochromatic photons with energy E_{in} impinge on the sample as shown in Fig. 1(b), the scan of the drain current I_c vs E_{in} gives a signal proportional to the x-ray absorption (XA) coefficient. The XA spectrum of Co metal at the $L_{2,3}$ edge is shown in Fig. 1(b). Let us now consider a more selective experiment where the energy of the scattered outgoing photons, E_{out}, is measured using a fixed incident-photon energy E_{in} at a suitable point in the absorption resonance. In this case one scans the outgoing intensity vs E_{out}, thereby obtaining a resonant scattering spectrum. For obvious analogy with traditional Raman, this approach is called resonant Raman scattering and it is also widely known under the name "resonant inelastic x-ray scattering" (RIXS). The RRS spectrum is thus a measurement of intensity vs E_{out} and reflects the existence of two decay channels in the soft x-ray region as mentioned above. Figure 1(c) shows the RRS spectrum of Co metal excited with incident photons of fixed energy at the L_3 absorption peak. The valence scattering $3d$-RRS in blue in Fig. 1(c) corresponds to the decay in blue in Fig. 1(a), while the inner-shell scattering $3s$-RRS in red in Fig. 1(c) corresponds to the decay in red in Fig. 1(a). In a more formal language, $3d$-RRS has the scattering path $2p^63d^n \to 2p^53d^{n+1} \to 2p^6(3d^n)^*$ and $3s$-RRS has the scattering path $2p^63d^n \to 2p^53d^{n+1} \to 2p^63s^13d^{n+1}$, where n is the $3d$ occupation in the ground state and the asterisk means either ground or excited state.

So far we have summarized the standard concepts since they are instrumental in introducing our approach.[18] Let us imagine measuring the total intensity of a given scattering channel, e.g., the intensity of the $3s$-RRS channel, i.e., the green area of the $3s$-RRS spectrum in Fig. 1(c). The total intensity I_a can be measured vs incident-photon energy E_{in}, thus obtaining the green spectrum in Fig. 1(d). For this reason we introduced the name "integrated RRS spectrum," i.e., $3s$-IRRS. Of course measuring the area of the $3d$-RRS gives the $3d$-IRRS spectrum. Thus IRRS is the measurement over a broad range of the scattered photons vs incident-photon energy E_{in} so that the total intensity of a selected scattering channel is observed without resolving the E_{out} dependence within that channel. The instrumental method for measuring the IRRS in a particular energy window is described in Sec. II D.

B. Magnetic circular dichroism in collinear and perpendicular geometries

Due to the integration over E_{out} and scanning vs E_{in}, the IRRS spectrum [Fig. 1(d)] resembles the XA spectrum [Fig.

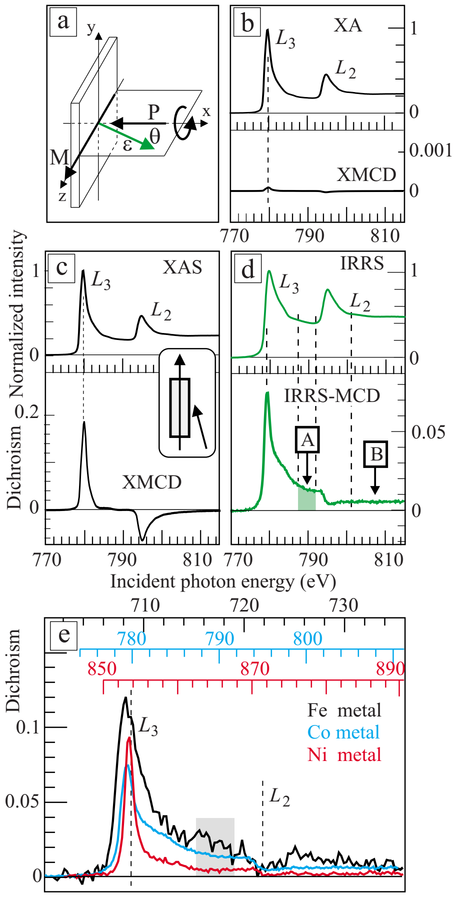

FIG. 2. (Color online) (a) Perpendicular geometry used in the RRS experiment (**M** is magnetization direction, **P** is helicity vector of incident x-ray photons, $\boldsymbol{\varepsilon}$ is emission direction, and θ is the angle between **P** and $\boldsymbol{\varepsilon}$). (b) Co $L_{2,3}$ and x-ray magnetic circular dichroism (XMCD) of Co metal measured in perpendicular geometry. (c) XA and XMCD of Co measured with x rays at 15° incidence to the magnetization direction. (d) $3s$-IRRS spectrum and corresponding IRRS magnetic circular dichroism (MCD) of Co obtained by reversing the circular polarization of the incident x rays. (e) $3s$-IRRS-MCD of Fe (black), Co (blue), and Ni (red) metals with corresponding color-coded incident-photon energy scales (in eV).

1(b)]. However both measurements provide different physical information because only the IRRS carries the signature of the scattering. This is particularly evident for magnetic samples in the so-called perpendicular geometry illustrated in Fig. 2(a). The sample is magnetized in plane along the surface and circularly polarized x rays are incident normal to the surface. In the experiment one measures the magnetic circular dichroism (MCD) where either the sample magnetization or the incident-photon helicity is reversed. Hereafter the dichroism spectrum is taken as the difference between the spectra with opposite polarizations of the incident x rays with a normalization factor given by the maximum of the sum of the two spectra.

In the perpendicular geometry [Fig. 2(a)], the XA measurements with left- and right-circularly polarized light are mirror symmetric so that the x ray magnetic circular dichroism (XMCD) is zero. In effect the measured XMCD in absorption is practically zero as shown in Fig. 2(b) with an upper limit of around 10^{-4}, demonstrating the good alignment of the apparatus [note the much expanded scale of the XMCD in Fig. 2(b)]. In order to measure for comparison the conventional XMCD in XA mode, a grazing incidence angle is used and the obtained Co $L_{2,3}$ XMCD is shown in Fig. 2(c). In a scattering experiment, the emitted photons are detected at an angle θ [Fig. 2(a)], which breaks the mirror symmetry so that a dichroism is observed upon reversal of the incident-x-ray polarization. This means that the perpendicular geometry allows MCD in the IRRS mode. This is what happens in the $3s$-IRRS measurements of Co shown in Fig. 2(d). We use $3s$-IRRS rather than $3d$-IRRS because the former gives a dichroism about ten times stronger than the latter.[18] The IRRS spectra and the IRRS dichroism were measured in scattering with $\theta=45°$ [green arrow in Fig. 2(a)], which gives maximum dichroism.

The IRRS dichroism is a consequence of the polarization of the core hole in the intermediate state after the $2p \rightarrow 3d$ absorption. We discuss in more detail the role of the core-hole polarization since it is a crucial part of the scattering process. Consider the excitation of a $2p$ core electron into an empty d-band state that has specific spin direction, e.g., caused by an applied field or exchange field. Due to the spin selection rule, $\Delta S=0$, the core hole created has the same spin direction as the annihilated valence-band hole. The orbital component obeys the selection rules $\Delta\ell=\pm 1$ with $\Delta m=q=1$ and -1 for left- and right-circularly polarized light, respectively, where q is the polarization component of the light. The transition probabilities are calculated from the Clebsch-Gordan coefficients with $q=1$ and -1, and this results in a distribution over the m_j sublevels of the j core levels that is far from uniform.[19] Sublevels with different $|m_j|$ values have a different angular shape. For the case of Fe, the calculated angular shape weighted over all m_j sublevels of the $j=3/2$ level in the geometry with $\mathbf{M}\|\mathbf{P}$ is shown in Fig. 3(a) for left- and right-circularly polarized light.[20] Their shape is cylindrical symmetric about the magnetization direction **M** and the photon helicity vector **P**, which are both collinear with the z axis. The q dependence of the core-hole shape can be directly understood from the optical selection rules. With $q=-1$ we create mainly $m_j=3/2$ holes, which have a positive quadrupole moment (charge density oriented along the z axis). With $q=1$ we create mainly $m_j=\pm 1/2$ holes, which have a negative quadrupole moment (charge density oriented on the xy plane). The dashed curve in Fig. 3(a) gives the difference, i.e., the core-hole shape corresponding to the XMCD. This shape of the core-hole distribution is given by even multipole moments with the maximum rank limited to the value of $2j$. This means that the $j=3/2$ state contains only a monopole and a quadrupole moment. The $j=1/2$ state cannot contain a quadrupole moment so that its shape is spherical symmetric. Figure 3(b) shows the expansion of the XMCD shape into a monopole and a quadrupole moment.

XMCD in XA is an angle-integrated measurement, which means that it is proportional to the monopole moment of the core hole. The difference between the volumes of the core-hole shape for the two polarizations (i.e., magnitude of the monopole moment in XMCD) can be related to the spin and orbital magnetic moments of the ground state, according to

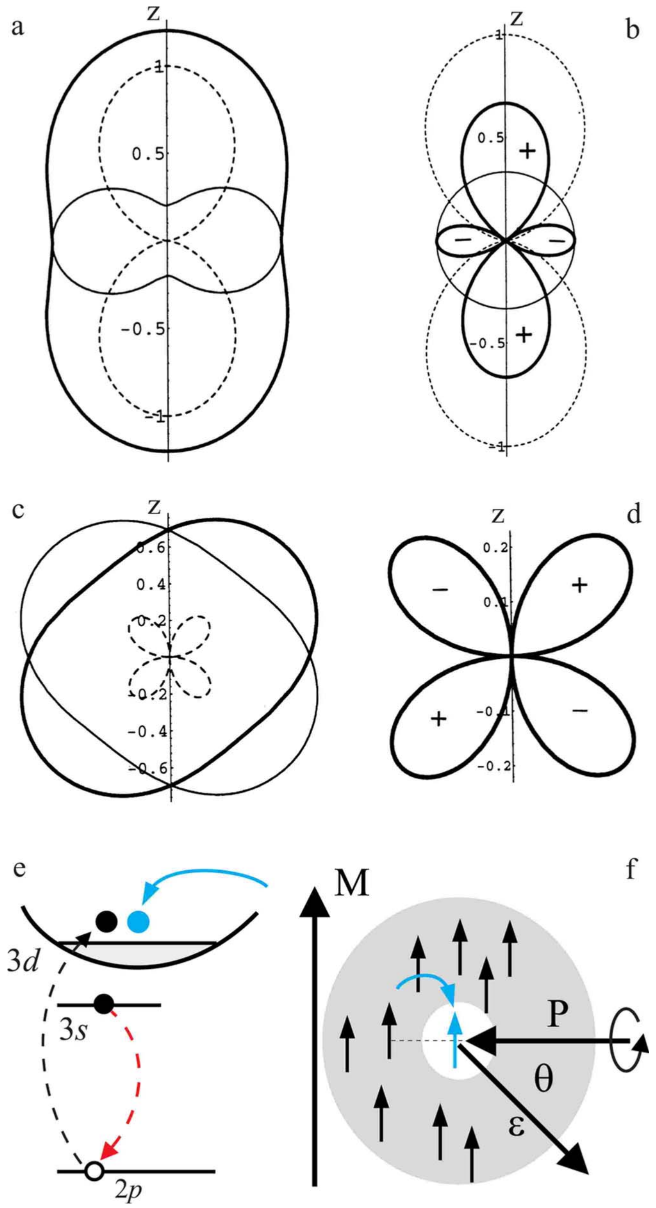

FIG. 3. (Color online) (a) Polarization of the $j=3/2$ core hole after $2p$ x-ray absorption in a $3d$ transition metal with spin-polarized valence band using light polarization $q=1$ (thin line), $q=-1$ (thick line), and the resulting difference, the XMCD (dashed line) for $\mathbf{M}\|\mathbf{P}$. (b) Decomposition of the XMCD contour (dashed line) into a monopole moment (thin line) and quadrupole moment (thick line). [(c) and (d)] Same for an angle between **M** and **P** of 90° where as seen the monopole contribution disappears. (e) Intermediate state of scattering where the core $2p$ hole is screened by an electron (blue) jumping in the core-hole site. (f) Schematic of the spin-dependent screening. Reversal of either the magnetization or the helicity of the x rays changes the angular distribution of the emission when the screening electron is spin polarized, hence resulting in MCD.

the XMCD sum rules.[21] The quadrupole moment of the $j=3/2$ level can also be related to the spin and orbital magnetic moments of the $3d$ states but with different coefficients.[22] In ferromagnetic materials the dominant contribution will come from the spin magnetic moment.

For a noncollinear geometry the core-hole shape is canted with respect to the z axis and the contribution of the quadrupole moment increases compared to the monopole moment. Figure 3(c) shows the core-hole polarization for an angle of 90° between **P** and **M**. In this transverse geometry, the monopole contribution disappears [see Fig. 3(d)], as it should be because the XMCD vanishes. This makes the transverse geometry ideal for measuring the quadrupole moment, which can be determined from the angular dependence of the emitted electrons or photons in the decay process following the absorption. The core-hole polarization model thus explains the presence of MCD in the x-ray scattering in perpendicular geometry and it relates its intensity to the ground-state magnetic moments. Obviously, we have described here a simple two-step model. The excitation step creates the core-hole polarization; the decay step monitors the core-hole polarization.[22,23]

The concept of IRRS dichroism presented above is the extension to photon scattering of the process seen in resonant photoemission, a "photon in-electron out" experiment, on Ni metal,[24] which is based on the same principle.[22,25] Note that the dichroism in perpendicular geometry in the IRRS mode has been used in the discussion of scattering sum rules.[26,27]

C. Femtosecond magnetism and the core-hole screening

Due to the core-hole polarization in the perpendicular geometry, it is not surprising that dichroism is seen in the incident-photon energy region of the $2p \rightarrow 3d$ transitions. Indeed the existence of a dichroism in perpendicular geometry is predicted by a simple local ionic model[22,28–32] without taking into account the evolution in the intermediate state of the scattering whose time scale is dictated by the core-hole lifetime. Note also that this model also predicts the absence of the dichroism at the L_2 edge. This rule is fully respected in an ionic case such as Co ferrite (see paper I). Also in the present case the minimum of the dichroism at L_2 is close to zero and is explained in this way. However the Co-IRRS dichroism in Fig. 2(d), reprinted from paper I, shows another piece of information which forms the experimental basis of the present discussion and which introduces the concept of the core-hole clock. In effect a dichroism is also observed at excitation energies well above the $2p \rightarrow 3d$ transitions, i.e., in an energy region where the conventional XMCD is zero [see Fig. 2(c)]. The data in Fig. 2(d) show a long tail of the IRRS dichroism in the regions between L_3 and L_2 (shaded green area labeled A) and above L_2 (region labeled B). In particular we concentrate on region A, which has the advantage that it is not affected by the Coster-Kronig conversion occurring in region B. There are two points to note in connection to this:

(i) The dichroism must originate from some process occurring in the intermediate state and inducing a polarization of the core hole; i.e., it must be due to some rearrangement in the intermediate state. In fact the transition from $2p$ to the εs state of the continuum, which is the only process in the absence of rearrangement, cannot polarize the core hole due to its lack of angular momentum.[22]

(ii) The dichroism is observed in metallic systems, while it is not found in magnetic insulators as shown in paper I.

Thus the rearrangement must be connected with the evolution of the Fermi sea in the presence of the core hole.

On this basis we explained this dichroism as the evidence of a core-hole polarization taking place via a spin-dependent screening during the lifetime of the core hole (on the order of femtosecond). This process is schematically represented in Figs. 3(e) and 3(f). In the intermediate state of the scattering process, the $2p$ core hole is screened by an extra $3d$ electron (in blue) jumping onto the site of the core hole. This is the situation of full screening. The screening electron [Fig. 3(f)] is polarized because the sample is magnetized so that the core hole becomes polarized. This polarization reverses for opposite magnetization $\mathbf{M}$ and is the origin of the $3s$-IRRS dichroism seen in the shaded areas of Figs. 2(d) and 2(e). This spin-dependent screening was treated theoretically by Chassé *et al.*[33] by applying it to the analogous process found earlier in resonant Auger emission.[34,35] The authors demonstrated theoretically that metallic Fe is fully screened in the intermediate state. In the present IRRS case we only have one shallow $3s$ core hole in the final state instead of two holes as in Auger, and this simplifies the picture. In Fig. 2(e) we present the $3s$-IRRS data along the Fe-Co-Ni metal series. The data are taken from paper I. The incident energy scales in the three cases (Fe in black, Co in blue, and Ni in red) are expanded and shifted in such a way that the position of the L_3 and L_2 peaks in the IRRS spectra coincide (vertical dashed lines). In this way the trend in the dichroism due to rearrangement in the intermediate state is clearly seen (gray shaded region). The relevant additional information is that Ni is not fully screened (or relaxed) in the intermediate state. If Ni would have been fully screened, then its magnetic moment would be almost zero (see also Sec. IV A 1) because the Ni impurity in this respect is similar to a Cu atom, where there is no magnetic moment. On the contrary, we see in Ni a sizable dichroism showing that the screening is not fast enough to reach full screening within the time scale dictated by the core-hole lifetime. This is a typical case of femtosecond magnetism explored using the core-hole clock effect.

Discussion of the above-mentioned effect would benefit from a dynamical model for deriving the screening time scale from the experiment. This model is presented in Sec. III, where we address the relation between the observed dichroism and the dynamics of the screening governed by the core-hole lifetime, the screening time, and the local magnetic moments with and without core hole. The model allows us under certain conditions to obtain the screening time scale from the experimental results but is not aimed to explain why the time constants are different in different systems. This latter point was discussed in paper I. The main idea is that a system such as Ni metal that has a narrow-band hole with large effective mass must relax around the core hole over a longer time scale. Unless otherwise stated the word *dichroism* refers in what follows to the dichroism due to spin-dependent screening.

D. Experimental information

The main experimental problem in IRRS is how the integration over the outgoing scattering channel is done. We used two equivalent methods for this purpose. In fact we have shown[36] that identical results are obtained with either a filter system[18] or a multilayer, where the latter gives more flexibility in the experimental setup. The integration over the $3s$ channel required in the $3s$-IRRS measurements can be done simply with a low-pass filter in front of a diode. The absorption edge of the filter must be between the $2p \rightarrow 3s$ and $2p \rightarrow 3d$ absorption edges so that the filter stops the $3d$-IRRS signal while the $3s$-IRRS is transmitted. An x-ray bandpass is not required since there is no other x-ray emission in the RRS spectrum as shown in Fig. 1(c). For a sample with a transition metal of atomic number Z, a convenient filter is a foil of atomic number $(Z-1)$ since the $L_{3,2}$ edge of the filter is above the $3s$ channel and below the $3d$ channel of the sample. Possible visible and UV emission is stopped by a thin Al foil (for more detail see Ref. 18). When using a multilayer on the other hand, the problem is to have a sufficiently large bandpass (say, 20–25 eV) in order to have sufficient integration over the selected scattering channel without a distortion of the IRRS spectrum. In fact a multilayer suitable for our energy range and with optimized reflectivity gives in general a too narrow bandpass. The appropriate bandpass is obtained using a spherical multilayer, i.e., with a focusing system that is deliberately mounted out of focus. The defocus is calculated analytically, tested by ray tracing, and checked experimentally with synchrotron radiation directly on the multilayer. It is noteworthy that in IRRS experiments the sensitivity is very high because the signal is strong due to integration so that also a tiny dichroism can be measured.[37]

For completeness we give some information on the measurements in paper I on Fe, Co, and Ni metals that we are interpreting here on the basis of our improved model. The samples were polycrystalline films evaporated *ex situ* (60 nm Co and Ni on Si and 7.5 nm Fe on MgO, 1 μm Co ferrite on MgO) and were measured as grown. Cleaning or evaporation *in situ* is not needed because the $3s$-IRRS is a bulk-sensitive "photon in-photon out" experiment. In any case for precaution the films were capped with 2 nm Au. All experimental work was done on beamline ID08 at the ESRF in Grenoble.

III. MODEL

A. Basic concepts

The general requirement that we impose in the construction of the model is a maximum simplicity compatible with a reasonable description of the process. This minimizes the number of parameters and hence reduces the ambiguities in the use of the model. In effect it is possible to image sophisticated models potentially more descriptive but this would involve parameters whose values will be very uncertain—to say the least. Therefore we assume that the dynamics of the screening is governed by a *linear-rate equation with only one time constant* τ_s *that we will call the "screening time constant."*

The model will be presented in the following sequence:

(i) We solve a suitable linear-rate equation for the nondecaying excited atom. The argument of this equation is the dichroism $D(t)$. In this way the screening time constant τ_s

enters the calculation together with the unscreened and screened magnetic moments μ_0 and μ_s.

(ii) We average $D(t)$ over the statistical ensemble of core holes probed in the experiment to obtain the measured dichroism D_m. In this way the core-hole lifetime τ_c, i.e., the time unit of our clock, enters the treatment.

The importance of the screening dynamics, i.e., the partial screening on appropriate time scales, was already stressed by Gunnarsson and Schönhammer[38] in the Auger emission and by Almbladh[39] in phonon relaxation observed in emission spectroscopy. A general discussion using a many-body ground state is given by Almbladh and Hedin.[40] Here we account for partial screening in magnetic IRRS spectroscopy in the same spirit although using a simplified approach. In fact we assume that the creation of the core hole is instantaneous and that the subsequent screening process is not influenced by the way in which the core hole is created. In this sense—but only in this sense—our model can be thought of as a two-step treatment. However this should not be confused with the traditional two-step models in which it is assumed that the system is fully relaxed in the intermediate state.

The derivation of the rate equation requires some care. In fact the model has to be compatible with the boundary conditions dictated by the physics of the process. The condition $D(0)=0$ is obvious since initially when the impurity is created the screening is not yet developed. In connection to this, it is crucial to remember that we are referring to the dichroism outside the region of the $2p \rightarrow 3d$ transitions, i.e., the dichroism which exists *only* after some spin-dependent screening has taken place. The boundary condition at very long time, i.e., $D(\infty)$, is more delicate. This condition is dictated by the numerical calculations of Chassé *et al.*[33] showing that in the sequence Fe, Co, Ni in a fully screened situation (i.e., in the asymptotic condition) the dichroism is proportional to the screened magnetic moment μ_s. In principle this restricts the treatment to cases where μ_s is sufficiently different from μ_0. In fact if $\mu_s=\mu_0$, i.e., in the absence of screening, we cannot assume that $D(\infty)$ is proportional to the moment. Otherwise a dichroism proportional to μ_0 would be developed also without screening, which is paradoxical. Thus our model cannot be extended to very weak screening close to the $\mu_s=\mu_0$ condition. In this case $D(\infty)$ is no longer proportional to μ_s and the description in Ref. 33 based on a linear muffin-tin orbital (LMTO) atomic sphere supercell local-density approximation (LDA) calculation needs to be improved. In the experiments discussed here, $\mu_0>\mu_s$ because the screening occurs by filling minority-spin states so that $\mu_0/\mu_s>1$. In practical terms the condition $\mu_s \neq \mu_0$ is not a serious limitation. In fact Fe complies with the linear dependence of $D(\infty)$ on μ_s so that Fe is within the safe region of the parameter space. On the other hand Fe is one of the cases where the screened and unscreened moments are closer together (we will show that $\mu_0/\mu_s=1.35$) so that most cases of practical interest can be treated by the present model. The precise estimation of the lower acceptable value of μ_0/μ_s, which is surely smaller than the Fe value of 1.35, is beyond the scope of the present work and would require a more sophisticated description of the screening. This would be conceptually interesting but adds very little to the practical applications of the model.

B. Introducing the model

Within the scheme outlined above, the magnetic moment μ of the "impurity" atom (i.e., the atom with the core hole) evolves in time according to the law

$$\frac{d\mu(t)}{dt} = \frac{-\mu(t)+\mu_s}{\tau_s}, \tag{1}$$

which has the well-known solution

$$\mu(t) = \mu_s + (\mu_0 - \mu_s)\exp(-t/\tau_s), \tag{2}$$

i.e., $\mu(t)$ changes exponentially from the initial not screened (unrelaxed) value $\mu(0)=\mu_0$ to the final fully screened asymptotic value $\mu(\infty)=\mu_s$. The time t is measured with the clock starting from the moment of the sudden creation of the core hole.

At each instant the variation in the core-hole polarization is proportional to a driving term, which is proportional to the difference between the actual polarization at time t and the asymptotic value at that instant, which in the spirit of the comments to Ref. 33 in Sec. III A must be proportional to $\mu(t)$ given in Eq. (2). For IRRS in transverse geometry the dichroism is proportional to the core-hole polarization, which is generated by a coupling to the spin of the screening charge. Therefore, the rate equation describing the evolution of the dichroism for a *nondecaying atom* with a core hole is

$$\frac{dD(t)}{dt} = \frac{-D(t)+C\mu(t)}{\tau_s}, \tag{3}$$

where C is a proportionality constant. Here we assume there is no delay in the adjustment of the core-hole polarization to the accumulation of the screening charge. Being an intra-atomic process, the adjustment is very fast and our approximation is legitimate. Substituting Eq. (2) into Eq. (3) and changing the proportionality constant $c=C/\tau_s$, one obtains

$$\frac{dD(t)}{dt} = -\frac{D(t)}{\tau_s} + c[\mu_s + (\mu_0-\mu_s)\exp(-t/\tau_s)]. \tag{4}$$

Solving Eq. (4) with the initial condition $D(0)=0$ gives

$$D(t) = c\mu_s\tau_s[1-\exp(-t/\tau_s)] + c(\mu_0-\mu_s)t\exp(-t/\tau_s). \tag{5}$$

To investigate the behavior of this dichroism, we write it as a function of t/τ_s and in units of the fully screened value,

$$D_s \equiv D(\infty) = C\mu_s = c\mu_s\tau_s. \tag{6}$$

Furthermore, we represent the properties of the sample by the parameter F defined as

$$F \equiv \frac{\mu_0}{\mu_s}. \tag{7}$$

The normalized dichroism for a *nondecaying atom* is then obtained as

$$\frac{D(t/\tau_s)}{D_s} = [1-\exp(-t/\tau_s)] + (F-1)\exp(-t/\tau_s)(t/\tau_s). \quad (8)$$

As can be verified, at $t=0$ the core hole is unscreened and the dichroism is zero, whereas for a time long compared to τ_s the core hole is screened and the normalized dichroism goes to 1. That is, the dichroism is proportional to μ_s as required by Eq. (6).

The expression in Eq. (8) contains two terms, both comprising an exponential decay. The first term represents a simple exponentially varying adjustment to the asymptotic values and we will call this the *adiabatical contribution* in the dichroism. Only the second term is dependent on F and contains a factor linearly dependent on t; hence we will associate this term with the *dynamical contribution* in the dichroism. Here, and in the following, we will keep track of these two contributions as this will provide mathematical insight into the functional behavior. Thus we have a sum of two functions: the first one, the adiabatical contribution, is fixed (i.e., independent of any parameters) and the second one, the dynamical contribution, scales with $F-1=(\mu_0-\mu_s)/\mu_s$, i.e., the change in the reduced magnetic moment. The latter contribution vanishes for $t\rightarrow 0$ and $t\rightarrow\infty$ and attains a maximum value of $(F-1)/e$ at $t=\tau_s$. Thus the maximum is proportional to the change in the reduced magnetic moment and occurs after a time equal to the screening time constant.

For the combined function in Eq. (8) the maximum is found as

$$\frac{D(t_{\max})}{D_s} = (F-1)\exp\left(-\frac{F}{F-1}\right)+1 \quad \text{at } t_{\max} = \frac{F}{F-1}\tau_s, \quad (9)$$

so that $t_{\max} > \tau_s$. The shape of the function in Eq. (8) is shown in the lower panel of Fig. 4 (black lines) for different F values. For a time t after core-hole creation much shorter than the screening time $(t \ll \tau_s)$, the dichroism increases linearly as Ft/τ_s. When t approaches τ_s, the behavior becomes much different for large and small values of F because the ratio between the dynamical and adiabatical contributions is proportional to $F-1$. For large F the dynamical contribution prevails and the maximum attains a value of about F/e at t just above τ_s. Thus for large F the maximum in the dichroism occurs at a time slightly longer than the screening constant time. The maximum is very pronounced and scales with F (see the black line for $F=20$ in the lower panel of Fig. 4). On the other hand at values of F not too high above 1 but still within the validity limit of the model, the adiabatical contribution prevails. For this case, Eq. (9) shows that the maximum extends marginally above the asymptotic value of 1 and shifts toward longer time, $t_{\max} \gg \tau_s$ (see the black line for $F=1.4$ in the lower panel of Fig. 4).

In the experiment one does not explicitly measure the time dependence of $D(t)$ but nonetheless observes the dynamical contribution because the measured quantity is a time integration over $D(t)$. In the experiment one accumulates information from many scattering events, each due to absorption of a single photon. Thus one measures an ensemble average taken over the surviving core-hole probability decaying with $\exp(-t/\tau_c)$, where τ_c is the core-hole lifetime (see Sec. III F for a salient point). Our experiment is, in fact, asynchronous and is not carried out as in the pump-probe mode. The latter manner could be a perspective for future x-ray lasers. The ensemble average, i.e., the measured dichroism D_m, can be expressed as the time average over the life span of a single impurity atom. This is equivalent to assuming that the system is ergodic. Thus the measured dichroism is

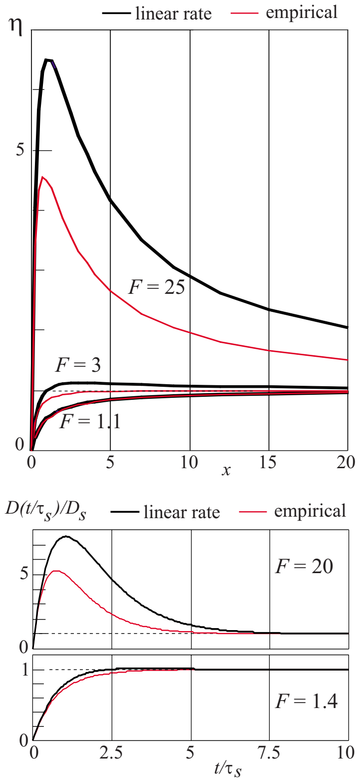

FIG. 4. (Color online) Lower panel: The universal function $D(t/\tau_s)/D_s$ in the present linear-rate model (black) given by Eq. (8) and the empirical function (red) used in paper I (Ref. 16) [Eq. (15) in present paper]. See text for further explanation. Upper panel: The dimensionless universal function $\eta(x)=D_m/D_s$, where $x=\tau_c/\tau_s$. Present model in black [Eq. (12)] and approximate model from paper I (Ref. 16) in red [Eq. (16) in present paper].

$$D_m = \frac{1}{\tau_c}\int_0^\infty D(t)\exp(-t/\tau_c)dt. \quad (10)$$

Once all other parameters and constants are known, the model defines a relation between the screening time constant τ_s and measured dichroism D_m. The exploitation of this relation is greatly simplified and the physics becomes more transparent if one relies upon the fact that the solution of Eq. (10) obeys a scaling law. This is suggested by the intuitive fact that the significant dependence of D_m is not on τ_s and τ_c separately but on their ratio

$$x \equiv \frac{\tau_c}{\tau_s}. \quad (11)$$

The final result is the reduced measured dichroism,

$$\eta(x) \equiv \frac{D_m}{D_s} = \frac{x}{x+1} + (F-1)\frac{x}{(x+1)^2} = \frac{(F+x)x}{(x+1)^2}, \quad (12)$$

which is universal within the validity limits of the model. In Eq. (12) we again separated the adiabatical and dynamical contributions. The adiabatical contribution $x/(x+1)$ increases monotonically from $\eta(0)=0$ to $\eta(\infty)=1$. The dynamical contribution $(F-1)x/(x+1)^2$ has $\eta(0)=\eta(\infty)=0$ and attains a maximum of $\eta=(F-1)/4$ at $x=1$, i.e., at $\tau_s=\tau_c$. The ratio between the dynamical and adiabatical contributions is $(F-1)/(x+1)$.

C. General properties of the model solutions

Consistent with the analytical results given above, the physical content of the model is apparent from the shape of the universal function $\eta(x)$ for various values of the parameter F. This is clear from Fig. 4 (upper panel), where the function η arising from the present model is given for various values of F by the solid black lines. Independent of F, all curves commence at zero, as required. For slow screening ($\tau_s \gg \tau_c$, i.e., $x \ll 1$) Eq. (12) simplifies to $\eta \approx Fx = (\mu_0/\mu_s)(\tau_c/\tau_s)$. In this case there is not enough time to fully screen the core hole before decay, so that reduced measured dichroism η is linear in τ_c/τ_s and μ_0/μ_s. When x becomes larger, this linear increase can no longer be sustained and at a certain point η will reach a maximum. There is a very strong dependence on F with quite different behaviors for low and high F values, reflecting the F dependence of the function $D(t)$ integrated with a weighting factor $\exp(-t/\tau_c)/\tau_c$ [cf. Eq. (10)]. Since 50% of the weight of this factor is below $0.69\tau_c$, the main contribution in η comes from the inclining part of the $D(t)$ function, which scales with F [Eq. (8)]. Finally, in the limit of fast screening ($\tau_s \ll \tau_c$, i.e., $x \to \infty$), the screening is complete before the core hole decays, and $D_m = D_s$, i.e., $\eta \to 1$.

For $F \le 2$ the η function increases monotonically toward the asymptotic value, whereas for $F > 2$ a maximum develops equal to

$$\eta(x_{\max}) = \frac{F^2}{4(F-1)} \quad \text{at } x_{\max} = \frac{F}{F-2}, \quad (13)$$

so that for large F the maximum is increasing approximately as $F/4$ with $x_{\max}$ slightly larger than 1. This situation, typical for large values of F, embodies in $\eta(x)$ the dynamical contribution in the dichroism. For large F the dynamical contribution dominates, giving a maximum in the canonical average when the screening time constant and core-hole lifetime are comparable (i.e., $x \approx 1$). This brings out the dynamical contribution to the dichroism in the η function because the weighting factor $\exp(-t/\tau_c)/\tau_c$ reduces the importance of $D(t)$ at longer time scales. Thus large F values show a high sensitivity to spin-dependent screening. This is obviously the case for Ni, which would have essentially no magnetic moment for a fully screened core hole, as we anticipated, so that F is large (see Sec. IV A 1).

Since the function η is not default monotonic, the retrieval of τ_s from the measured dichroism is not always straightforward, even when the parameters involved in the model are known. If η is monotonic ($F \le 2$), the inverse function is injective; i.e., it is a one-to-one function. For $F > 2$ the function η is not monotonic and returns two possible values of τ_s for a given function value. In general, this would require a supplementary condition to select the correct solution [see Sec. IV for a discussion of the experimental results in Fig. 2(e) and the case of the magnetic impurities].

D. Comparison with the old model

The old model put forward in paper I was not obtained from a differential equation but was simply based on a sensible conjecture for the shape of the function $D(t)$. We introduced an approximate function $D(t)$ by multiplying an exponential increase toward 1 by the evolution of the magnetic moment given in Eq. (2). Thus instead of the solution in Eq. (5) of our differential equation in Eq. (4), we used what we will call the empirical expression,

$$D(t) = C[1 - \exp(-t/\tau_s)][\mu_s + (\mu_0 - \mu_s)\exp(-t/\tau_s)], \quad (14)$$

which in the normalized form is

$$\frac{D(t/\tau_s)}{D_s} = [1 - \exp(-t/\tau_s)] + (F-1)\exp(-t/\tau_s)[1 - \exp(-t/\tau_s)]. \quad (15)$$

This conjecture retains the basic physics of the description. In fact the normalized dichroism respects the boundary conditions for $t \to 0$ and $t \to \infty$ and it is expressed as the sum of the same adiabatical contribution and, with the same coefficient $(F-1)$, of a dynamical contribution giving a maximum at an intermediate time. For $t \ll \tau_s$ the dichroism increases linearly as Ft/τ_s in the same way as in the linear-rate model (Sec. III B). The dynamical contribution, on the other hand, differs from that in the linear-rate model and can give a substantial deviation. The dynamical contribution has a maximum at $t_{\max} = \tau_s \ln 2 \approx 0.69\tau_s$ in the empirical expression [Eq. (15)], instead of at $t_{\max} = \tau_s$ in the linear-rate model. Furthermore, its maximum value is $(F-1)/4$ in the empirical expression, which is smaller than the value $(F-1)/e$ in the linear-rate case. In fact inspection shows that $(-t/\tau_s)$ in Eq. (8) is replaced by $[1 - \exp(-t/\tau_s)]$ in Eq. (15), which means that the latter function has always a lower value, be it that for $t \ll \tau_s$ and $t \to \infty$ both functions become equal. The differences between both functions are clearly seen in Fig. 4 (bottom panel), which shows the comparison between the function $D(t/\tau_s)/D_s$ from Eq. (8) (black curve) and the empirical one in Eq. (15) (red curve) for $F=1.4$ and $F=20$. The difference between both models is marginal for low F since the adiabatical term prevails, while for high F the dynamical term prevails, leading to a large discrepancy.

Inserting Eq. (15) into the integral of Eq. (10), one obtains an empirical expression for D_m which also in this case, as done in paper I, can be cast into a universal form, i.e.,

$$\eta(x) = \frac{x}{x+1} + (F-1)\frac{x}{(x+1)(2x+1)} = \frac{x(F+2x)}{(x+1)(2x+1)}. \tag{16}$$

As a consequence of the different properties of $D(t/\tau_s)/D_s$, the empirical $\eta(x)$ function will differ from the linear-rate solution. The behavior for slow screening ($\tau_s \gg \tau_c$, i.e., $x \ll 1$) is nevertheless the same: the function η increases linearly as Fx. Also for fast screening ($\tau_s \ll \tau_c$, i.e., $x \to \infty$) we have $\eta \to 1$ because the adiabatical contribution is the same. However the dynamical contribution is different. Its maximum is found at $x=1/\sqrt{2}$ instead of at $x=1$ so that the maximum of $\eta(x)$ is at smaller x for the empirical expression than for the linear-rate expression. The empirical $\eta(x)$ curves are plotted in red in the upper panel of Fig. 4 and are compared with the linear-rate functions in black. Obviously, the error in the $\eta(x)$ function is considerable for large F, although the general shape is quite similar. We stress the following points:

(i) The changeover from monotonic to nonmonotonic functions occurs at $F=3$ in the empirical model, instead of $F=2$. We will see that this difference is very important in the analysis of the Co metal data supporting the linear-rate model (see Sec. IV A 2).

(ii) For large F the η values at the right-hand side of the maximum in the empirical model are strongly underestimated. For example, with $F=25$ and $\eta=3$ the value of x is underestimated by a factor of about 2. We show the importance of this aspect in the case of magnetic impurities in Sec. IV B.

E. Evaluating the *F* value

The F value, representing the properties of the sample, is very crucial in the analysis and requires an independent evaluation of μ_0 and μ_s. The moment μ_0 is by definition the ground-state moment, which is in general known from a variety of experimental methods. Moreover, there are reliable calculations supporting these values. More delicate is the evaluation of μ_s, which is a somewhat exotic parameter, i.e., the moment of the atom in the presence of the core hole and fully screened in the solid. This can be evaluated in two ways, or with the combination of both:

(i) Via direct calculation as in the case of Fe, Co, and Ni metals in Ref. 33. Modern computational methods allow reliable results to be obtained. However, results of this kind are not generally available and specific calculations might be required.

(ii) Via the $Z+1$ approximation based on the fact that an atom with a core hole is essentially an atom with an atomic number of $Z+1$. For example, the value of μ_s in Ni is fairly well approximated by the ground-state moment of a Cu impurity in Ni. The values of impurities moments are generally known from experiments and also numerous calculations are available. Note that the $Z+1$ approximation does not give in general satisfactory density of states but works fairly well in giving an integral property as the moment.[33]

F. Competing decay channels

In practice the core hole decays by several competing processes to different final states. The 3s-IRRS is measured using the $3s \to 2p$ decay channel, which is much less probable than the Auger channel. In our theory we use the lifetime of the intermediate state determined by the sum of all the decay probabilities, i.e., the lifetime corresponding to the total linewidth of the intermediate state with a $2p$ hole. This is correct for the following reasons.

In the measurement of a spectrum, we observe the decay of a large number of core holes so that we are averaging over a canonical ensemble of holes. In this ensemble we consider the decay scheme where two decay channels are in competition (branching between two channels): (i) the Auger channel with a decay probability per unit time p_1 and (ii) the photon emission channel (radiative channel) with a decay probability per unit time p_2, where the Auger channel has a much larger probability, i.e., $p_1 \gg p_2$. The decay probabilities are proportional to the partial widths of the levels tabulated in the literature (see, e.g., Ref. 41). Note that the two decays (Auger and radiative) are mutually exclusive events so that the total decay probability of the core hole is the sum of p_1 and p_2. Let us have, at $t=0$, N_0 core holes. The core-hole decay rate is $dN=-(p_1+p_2)Ndt$, giving an exponential solution. The fraction of holes emitting a photon is $dN_2 = [p_2/(p_1+p_2)]dN$, so that $N_2(t)=[p_2/(p_1+p_2)]N(t)$. These relations produce an exponential decay with a decay rate due to the *total* linewidth. The fact that the radiative channel has a low probability means that fewer photons are emitted but it does not mean that the intermediate state is sampled with a longer time constant. It means a different intensity and not a different time scale. Therefore, the internal core-hole clock is the same for both channels.

An illustrative model at macroscopic scale can be given by considering a water basin that is emptied by releasing water simultaneously through two tap holes with very different diameters: a small hole representing the "radiative" channel and a large hole representing the "Auger" channel. The time it takes before the basin is empty is the same for both holes and can be measured by observing the flux through either the small hole or the large hole. Of course, we have a much smaller "signal" by monitoring the small hole. Another much more precise analogy can be found in the decay of a set of radioactive nuclei with two (or more) decay channels in competition, which is formally the same problem.[42]

IV. DISCUSSION

A. Fe, Co, and Ni metal cases

The present model gives a rationale for the trend of the measured dichroism in Fe, Co, and Ni metals shown in Fig. 2(e). We refer of course to the dichroism outside the $2p \to 3d$ transitions, i.e., the dichroism, represented by the shaded areas in Fig. 2(e), induced by spin-dependent screening. In order to reduce the effect of self-absorption and saturation, we use the flipping ratio $(I^+-I^-)/(I^++I^-)$ instead of the dichroism I^+-I^-, which is the difference between the IRRS spectra I^+ and I^- taken with opposite circular polarizations. In paper I we used the fact that Fe is practically fully screened in the intermediate state, as shown by the analysis of the Auger spectra.[33] Moreover, we used the fact that the dichroism (and hence the flipping ratio) in the fully screened

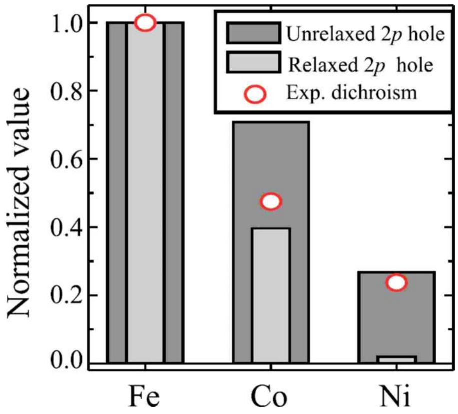

FIG. 5. (Color online) Measured flipping ratio (red circles) in the dichroism due to spin dependent screening [energy region between L_3 and L_2 labeled by A in Fig. 2(d)] for Fe, Co, and Ni metals. Magnetic moments of the 3d states with screened (relaxed) and unscreened (unrelaxed) $2p_{3/2}$ core hole. All values are normalized to unity in Fe metal. Reprinted from paper I (Ref. 16).

situation is proportional to μ_s.[33] On this basis it is useful to compare as done in Fig. 5, reprinted from paper I, the trend with Z of the measured flipping ratio (red dots) of the unrelaxed (unscreened) and relaxed (screened) moments, having normalized each of these quantities to 1 in Fe. This was very convincing evidence that Ni experimental result is considerably away from the fully screened situation.

The present model allows a deeper insight into the analysis than in our previous work in paper I. The analysis is summarized in Fig. 6 and is based on the arguments given below. The numerical results are collected in Table I.

1. Nickel

In Ni metal the value of $F = \mu_0/\mu_s$ is very high because the screened moment μ_s in the presence of the core hole is very small. According to the calculations in Ref. 33, the F value due to the 3d states is 18, while in the $Z+1$ approximation the calculations by Zeller[43] gave $F=20$, in good agreement. Those numbers should be regarded as a lower limit of a value that can even be larger because of the reduction in μ_s due to the sp contribution. In spite of this uncertainty the model analysis is rather safe. In effect, Fig. 6 suggests as in paper I that the measured flipping ratio is at least seven times the relaxed value. The most likely value from a detailed data analysis is around 9 as shown by the gray shaded area in Fig. 6 (upper panel). The theoretical η curve going through this area corresponds to $F=35$, which is fully compatible with the above evaluations. The value of $x = \tau_c/\tau_s$ will be around 1.1, so that the screening time constant is $\tau_s = \tau_c/1.1 = 1.5$ fs, using $\tau_c = 1.65$ fs according to Ref. 41. This result is rather stable against the variation in the parameters. In effect, the theoretical peak is very sharp so that an even larger F would give a narrow range of x between the two intersections with the horizontal line at $\eta=9$. In conclusion, the value of τ_s compatible with the experiment is between 0.8 and 2.5 fs.

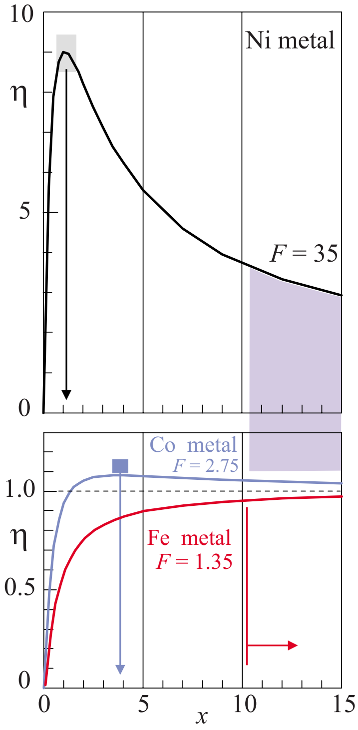

FIG. 6. (Color online) Analysis of the experimental results in Fig. 2(e) using the present linear-rate model: the η functions appropriate to Ni (black curve), Co (blue curve), and Fe (red curve) metals. The color-coded arrows indicate the values obtained for $x = \tau_c/\tau_s$ in the three metals. See text for further explanation.

2. Cobalt

In Co metal the F value is obviously much lower than in Ni. According to the calculations in Ref. 33 and the $Z+1$ approximation with the calculations in Ref. 44, one obtains $F=2.75$, yielding the theoretical blue line in the lower panel of Fig. 6. Note that the curve is nonmonotonic and predicts a small increase in the dichroism with respect to the relaxed value. As a matter of fact this is the case of the experiment giving a 12–18 % increase, as shown by the blue area in Fig. 6. There is remarkable agreement if we consider the numerous uncertainties (in effect the curve with $F=2.95$ would go through the shaded blue area). Thus $x=3.9$ and the screening time constant is $\tau_s=0.43$ fs, with confidence interval between 0.41 and 0.45 fs [$\tau_c=1.7$ fs in Co (Ref. 41)]. In conclusion, as apparent at a glance from Fig. 6, there is a difference of about a factor of 4 in screening speed for Co metal compared to the slower Ni case. Note that the fitting of the Co would be clearly impossible with the old model in paper I. In fact, any reasonable F value is <3, so that the old approximate η function would be monotonic and always lower than 1. Thus it would be impossible to explain the

TABLE I. Summary of the results for Fe, Co, and Ni metals. The spin-dependent screening time constants τ_s are given in femtoseconds.

	$F \equiv \mu_0/\mu_s$	$x \equiv \tau_c/\tau_s$	τ_s (best value)	τ_s (range)	Notes
Fe	1.35	>10	<0.18	<0.18	See Ref. 47
Co	2.75	3.9	0.43	0.41–0.45	
Ni	35	1.1	1.5	0.8–2.5	

increased dichroism observed in Co with respect to the asymptotic value.

3. Iron

Without much doubt F is even smaller in Fe. According to the calculations in Ref. 33 and the $Z+1$ approximation with calculations[45] and experiments,[46] one has $F=1.35$. Thus in any case the curve is monotonic and lower than 1. Since Fe is assumed to be completely screened in the intermediate state[33] and by considering the error bars, x would be as in Fig. 6 in any case larger than 10. Thus τ_s is below 0.18 fs, since $\tau_c=1.8$ fs (see Ref. 41). In this case the analysis permits only an upper limit for τ_s. See below for the possibility of obtaining more detailed information in a different IRRS experiment.

B. Perspectives

The more transparent interpretation opens up further perspectives. Here we discuss briefly only some of the more immediate implications after having stressed that any systematic experiment on magnetic alloys can be useful both to improve the model, if necessary, and to measure the screening time which is one of the fastest processes involved in magnetism and which is hardly accessible by other methods. In this context a promising case would be that of magnetic impurities (element A) diluted in a magnetic metal B. In our interpretation scheme the screening constant is a dynamical property of the majority component B and is only little, if at all, affected by the impurity. Thus as a first approximation it is possible to compare directly the elemental system A with the impurity A diluted in B having changed only the screening constant. In conclusion, it will be possible to selectively observe the effect of the change in τ_s.

Let us consider, e.g., Ni impurities in Fe. Also in this case the screened value μ_s is obviously very small so that the representative point of Ni slides essentially along the same curve considered for Ni metal in Fig. 6. Here, there is no ambiguity and the point slides toward the right to match the τ_s value of the majority component, which is Fe. Thus the representative point is in the purple shaded region in Fig. 6, and a substantial decrease in the Ni dichroism is expected due to the much faster and more effective screening in the intermediate state. Moreover the measured reduction in η defines the value of x, which in turn gives the screening constant of Fe, which cannot be determined by a simple experiment on elemental Fe, as shown above.[47] In essence, it is possible to use a magnetic impurity to probe the characteristic screening time of the majority component.

V. CONCLUSIONS

In a core-hole excitation in a magnetic metal, the incoming x rays suddenly create an impurity that is screened in a spin-dependent way. A scattering experiment in the L_3 region which, at a symmetry-breaking emission angle, observes the total intensity of the decay channel terminating with a $3s$ hole has already been shown to give information on the time scale of this screening process. In the current paper we have presented a linear-rate model for use in the analysis of these experiments and we have applied this to Ni, Co, and Fe metals. This model based on a differential equation replaces our previous empirical model and is able to produce quantitative results that cannot be obtained by the previous model. In particular the screening time constant is longer in Ni, with a value between 0.8 and 2.5 fs (with 1.5 fs as the most likely value) that is definitely larger than in Fe, which is presumably due to a narrow-band effect. In Co the screening time is slightly above 0.4 fs, while in Fe we find an upper limit of 0.18 fs. Moreover, the model shows the importance of future experiments on diluted magnetic impurities. An interesting effect is observed in Ni and to a lesser degree in Co. In these cases the measured dichroism exceeds the value expected in the case of complete screening of the core hole in the intermediate state. In other words when the core-hole decay provides insufficient time to reach the full screening, there is an enhancement of the dichroism. In agreement with the experiment, the model explains this effect and clarifies that this is particularly important when the screening time and core-hole lifetime are comparable in size in systems where the screened and unscreened magnetic moments are very different. More precisely the model shows that this effect cannot take place if the ratio of the unscreened to screened magnetic moment is smaller than 2.

In general, experiments as those discussed here provide unique information on the spin-dependent response of the Fermi sea to the creation of an impurity and in general to the perturbation at an atomic site. The present approach based on x-ray Raman scattering with information on the femto- and attosecond time scales will cross-fertilize with future measurements utilizing pulsed sources including free-electron lasers and desktop attosecond lasers.

ACKNOWLEDGMENTS

L.B. wants to thank A. Tagliaferri and V. Bisogni for stimulating discussions.

---

[1] E. Beaurepaire, J.-C. Merle, A. Daunois, and J.-Y. Bigot, Phys. Rev. Lett. **76**, 4250 (1996).

[2] M. Aeschlimann, M. Bauer, S. Pawlik, W. Weber, R. Burgermeister, D. Oberli, and H. C. Siegmann, Phys. Rev. Lett. **79**, 5158 (1997).

[3] H.-S. Rhie, H. A. Dürr, and W. Eberhardt, Phys. Rev. Lett. **90**, 247201 (2003).

[4] M. Lisowski, P. A. Loukakos, A. Melnikov, I. Radu, L. Ungureanu, M. Wolf, and U. Bovensiepen, Phys. Rev. Lett. **95**, 137402 (2005).

[5] B. Koopmans, J. J. M. Ruigrok, F. Dalla Longa, and W. J. M. de Jonge, Phys. Rev. Lett. **95**, 267207 (2005).

[6] M. Cinchetti, M. Sánchez Albaneda, D. Hoffmann, T. Roth, J. P. Wüstenberg, M. Krauszs, O. Andreyev, H. C. Schneider, M. Bauer, and M. Aeschlimann, Phys. Rev. Lett. **97**, 177201 (2006).

[7] C. Stamm, T. Kachel, N. Pontius, R. Mitzner, T. Quast, K. Holldack, S. Khan, C. Lupulescu, E. F. Aziz, M. Wietstruk, H. A. Dürr, and W. Eberhardt, Nature Mater. **6**, 740 (2007).

[8] A. Melnikov, H. Prima-Garcia, M. Lisowski, T. Gieszel, R. Weber, R. Schmidt, C. Gahl, N. M. Bulgakova, U. Bovensiepen, and M. Weinelt, Phys. Rev. Lett. **100**, 107202 (2008).

[9] C. D. Stanciu, F. Hansteen, A. V. Kimel, A. Kirilyuk, A. Tsukamoto, A. Itoh, and Th. Rasing, Phys. Rev. Lett. **99**, 047601 (2007).

[10] I. Žutić, J. Fabian, and S. Das Sarma, Rev. Mod. Phys. **76**, 323 (2004).

[11] P. B. Corkum and F. Krausz, Nat. Phys. **3**, 381 (2007), and references therein.

[12] G. Sansone, E. Benedetti, F. Calegari, C. Vozzi, L. Avaldi, R. Flammini, L. Poletto, P. Villoresi, C. Altucci, R. Velotta, S. Stagira, S. De Silvestri, and M. Nisoli, Science **314**, 443 (2006).

[13] M. Uiberacker, Th. Uphues, M. Schultze, A. J. Verhoef, V. Yakovlev, M. F. Kling, J. Rauschenberger, N. M. Kabachnik, H. Schröder, M. Lezius, K. L. Kompa, H.-G. Muller, M. J. J. Vrakking, S. Hendel, U. Kleineberg, U. Heinzmann, M. Drescher, and F. Krausz, Nature (London) **446**, 627 (2007).

[14] A. L. Cavalieri, N. Müller, Th. Uphues, V. S. Yakovlev, A. Baltuška, B. Horvath, B. Schmidt, L. Blümel, R. Holzwarth, S. Hendel, M. Drescher, U. Kleineberg, P. M. Echenique, R. Kienbergel, F. Krausz, and U. Heinzmann, Nature (London) **449**, 1029 (2007).

[15] The possibility of working in the x-ray regime with both attosecond lasers and free-electron lasers is discussed in Ref. 11.

[16] L. Braicovich, G. Ghiringhelli, A. Tagliaferri, G. van der Laan, E. Annese, and N. B. Brookes, Phys. Rev. Lett. **95**, 267402 (2005); **99**, 159902(E) (2007).

[17] P. A. Brühwiler, O. Karis, and N. Mårtensson, Rev. Mod. Phys. **74**, 703 (2002), and references therein.

[18] L. Braicovich, G. van der Laan, G. Ghiringhelli, A. Tagliaferri, and N. B. Brookes, Phys. Rev. B **66**, 174435 (2002).

[19] G. van der Laan, Lect. Notes Phys. **697**, 143 (2006).

[20] G. van der Laan, J. Electron Spectrosc. Relat. Phenom. **101-103**, 859 (1999).

[21] G. van der Laan, Phys. Rev. B **57**, 112 (1998).

[22] G. van der Laan and B. T. Thole, J. Phys.: Condens. Matter **7**, 9947 (1995).

[23] M. van Veenendaal, P. Carra, and B. T. Thole, Phys. Rev. B **54**, 16010 (1996).

[24] B. T. Thole, H. A. Dürr, and G. van der Laan, Phys. Rev. Lett. **74**, 2371 (1995).

[25] G. van der Laan and B. T. Thole, Phys. Rev. B **52**, 15355 (1995).

[26] L. Braicovich, A. Tagliaferri, G. van der Laan, G. Ghiringhelli, and N. B. Brookes, Phys. Rev. Lett. **90**, 117401 (2003).

[27] An excellent summary on scattering sum rules and in general on the dichroism in perpendicular geometry is given by W. Schülke, *Electron Dynamics by Inelastic X-Ray Scattering* (Oxford University Press, Oxford, 2007), p. 467.

[28] P. Ferriani, C. M. Bertoni, and G. Ferrari, Phys. Rev. B **69**, 104433 (2004).

[29] K. Fukui, H. Ogasawara, A. Kotani, T. Iwazumi, H. Shoji, and T. Nakamura, J. Phys. Soc. Jpn. **70**, 1232 (2001).

[30] K. Fukui, H. Ogasawara, A. Kotani, T. Iwazumi, H. Shoji, and T. Nakamura, J. Phys. Soc. Jpn. **70**, 3457 (2001).

[31] M. Taguchi and G. van der Laan, Phys. Rev. B **66**, 140401(R) (2002).

[32] M. Taguchi, G. van der Laan, E. Arenholz, S. S. Dhesi, and E. Dudzik, Phys. Rev. B **68**, 104408 (2003).

[33] A. Chassé, H. A. Dürr, G. van der Laan, Yu. Kucherenko, and A. N. Yaresko, Phys. Rev. B **68**, 214402 (2003).

[34] G. van der Laan, H. A. Dürr, and M. Surman, J. Electron Spectrosc. Relat. Phenom. **78**, 213 (1996).

[35] H. A. Dürr, G. van der Laan, D. Spanke, F. U. Hillebrecht, and N. B. Brookes, J. Electron Spectrosc. Relat. Phenom. **93**, 233 (1998).

[36] L. Braicovich, G. van der Laan, A. Tagliaferri, E. Annese, G. Ghiringhelli, and N. B. Brookes, Phys. Rev. B **75**, 184408 (2007).

[37] The statistical noise is a stringent limitation in MCD experiments in perpendicular geometry in the RRS mode, i.e., with energy resolution in both incident and scattered beams. See L. Braicovich, G. van der Laan, G. Ghiringhelli, A. Tagliaferri, M. A. van Veenendaal, N. B. Brookes, M. M. Chervinskii, C. Dallera, B. De Michelis, and H. A. Dürr, Phys. Rev. Lett. **82**, 1566 (1999); and M. Taguchi, L. Braicovich, E. Annese, C. Dallera, G. Ghiringhelli, A. Tagliaferri, and N. B. Brookes, Phys. Rev. B **69**, 212414 (2004).

[38] O. Gunnarsson and K. Schönhammer, Phys. Rev. B **22**, 3710 (1980).

[39] C.-O. Almbladh, Phys. Rev. B **16**, 4343 (1977).

[40] C.-O. Almbladh and L. Hedin, in *Handbook on Synchrotron Radiation*, edited by E. E. Koch (North-Holland, Amsterdam, 1983), Vol. 1, p. 607.

[41] O. Keski-Rahkonen and M. O. Krause, At. Data Nucl. Data Tables **14**, 139 (1974).

[42] *Experimental Nuclear Physics*, edited by E. Segrè (Wiley, New York, 1959), Vol. 3, Sec. 2, pp. 7–8.

[43] R. Zeller, J. Phys. F: Met. Phys. **17**, 2123 (1987).

[44] V. S. Stepanyuk, R. Zeller, P. H. Dederichs, and I. Mertig, Phys. Rev. B **49**, 5157 (1994).

[45] B. Drittler, N. Stefanou, S. Blügel, R. Zeller, and P. H. Dederichs, Phys. Rev. B **40**, 8203 (1989).

[46] N. Janke-Gilman, M. Hochstrasser, and R. F. Willis, Phys. Rev. B **70**, 184439 (2004), and references therein.

[47] Experiment on Ni impurities in Fe was done recently by A. Tagliaferri, V. Bisogni, and N. B. Brookes (private communication). These authors found a reduction in Ni dichroism by a factor of about 3, which would give $x=15$ with τ_s of Fe around 0.1 fs.